atmosphere

MDPI

Article

Molecular Kinetic Simulations of Transient and Steady Wave Propagation into a Planet's Exosphere

Lucia Tian [1], Robert E. Johnson [2,3,*], Orenthal J. Tucker [4], Adam K. Woodson [3], Hayley N. Williamson [5] and Shane R. Carberry Mogan [6]

1 Department of Astronomy, University of Virginia, Charlottesville, VA 22904, USA
2 Department of Physics, New York University, New York, NY 10003, USA
3 Department of Materials Science & Engineering, University of Virginia, Charlottesville, VA 22904, USA
4 NASA Goddard Space Flight Center, Greenbelt, MD 20771, USA
5 Swedish Institute of Space Physics, 98192 Kiruna, Sweden
6 Space Sciences Laboratory, University of California, Berkeley, Berkeley, CA 94720, USA
* Correspondence: rej@virginia.edu

Abstract: The vertical propagation of wave energy into a planet's exosphere, a process that affects atmospheric evolution, is calculated here using 1D molecular kinetic simulations. Effects sensitive to molecular interactions are examined by comparing simulation results to solutions of linear fluid models for steady wave activity using parameters associated with Mars' upper atmosphere. In addition to correctly describing the wave behavior in the exobase region, these simulations directly yield nonlinear effects such as atmospheric heating. They also readily include the transient behavior due to the onset and decay of waves propagating into the rarefied region of a planet's atmosphere. This is a first step in understanding the effects of variable wave activity in the region where the atmosphere evolves from collisional to collisionless.

Keywords: molecular kinetics; atmospheric waves; planetary exospheres

Citation: Tian, L.; Johnson, R.E.; Tucker, O.J.; Woodson, A.K.; Williamson, H.N.; Mogan, S.R.C. Molecular Kinetic Simulations of Transient and Steady Wave Propagation into a Planet's Exosphere. *Atmosphere* **2023**, *14*, 441. https://doi.org/10.3390/atmos14030441

Academic Editors: Erdal Yiğit, Alexander Medvedev, Shuanggen Jin, Ed Thiemann and Jun Cui

Received: 11 January 2023
Revised: 20 February 2023
Accepted: 21 February 2023
Published: 23 February 2023

1. Introduction

The physics of the exobase region in the upper atmosphere of a planetary body plays a critical role in determining its long-term evolution by affecting the interaction with its space environment and the rate of atmospheric escape. The response to a disturbance in this region is sensitive to the transition from a fluid-like, collision-dominated gas, typically studied in the gravity wave literature, to a nearly collisionless corona. Therefore, the large-amplitude perturbations observed to propagate into the exospheres on both Mars and Titan, e.g., [1–7], are of interest as they can cause heating or cooling in the thermosphere, which, in turn, affects the exobase altitude and escape rate [7,8]. Although perturbations in this region can be produced by external processes such as solar events, the time-varying perturbations observed are often interpreted as upwardly propagating gravity waves, e.g., [2,9].

In the perturbed rarefied regions of the Mars and Titan atmospheres, the vertical wavelengths observed in the density along the 1D spacecraft trajectory and the atmospheric scale height are often readily extracted, e.g., [1,6,9]. However, such data are insufficient to correctly describe the heating produced by wave activity in the upper atmosphere, especially in the region in which collisions become rare and fluid models are inapplicable [10–13]. This is a region of interest to us when interpreting in situ spacecraft and remote sensing observations.

Fortunately, molecular kinetic (MK) simulations have been shown to correctly describe the rarefied region of a planet's atmosphere, e.g., [11,12]. Therefore, such simulations are used here to model wave-like perturbations with amplitudes suggested by the observations of the upper atmospheres of Mars and Titan. In MK simulations, intermolecular collisions

are directly modeled so that thermal conductivity, viscosity, and the resultant heating are accounted for. By specifying the conditions at the lowest altitude of the simulation domain, the density profiles, temperature profiles, and net heating or cooling vs. altitude can be uniquely modeled even if the atmosphere is not in local thermal equilibrium. Since gravity simply confines the molecular trajectories or allows escape, the transition region and the upper boundary are accurately treated, as has been noted often. Although such simulations can require enormous computational effort if extended over too large a range of densities, they are needed to correctly describe the rarefied region of an atmosphere and escape. This is the case even in the transition region below the nominal exobase, in which the mean free path between collisions is a small fraction of the scale height [12,14].

In order to describe the effect of the onset of wave perturbations in the important rarefied region, one-dimensional (1D) MK simulations of acoustic waves in the transition region of a Mars-like upper atmosphere were carried out in [13], hereafter referred to as L20. Using the Direct Simulation Monte Carlo (DSMC) method [15], which is equivalent to solving the Boltzmann equation, L20 compared the effects of density pulses, thermal pulses, and wave activity driven from a lower simulation boundary. In all cases, they showed that extracting a temperature profile from an in situ spacecraft density profile, which is the typically used process [1], can be problematic in the presence of such activity. This problem was subsequently elaborated on in [10] using a 2D linear analytic fluid model (LAFM).

Here, we expand on the work in L20 by also using the well-established DSMC method [15] to simulate the vertical and temporal propagation of wave-like perturbations driven from a lower boundary in a simple model upper atmosphere. Although multidimensional wave activity can certainly be described using the MK method, our goal in this paper is to understand the effects of wave propagation into the rarefied region. We examine the effect of frequency and background properties on the transient behavior, as well as on the vertical propagation and heating, in the exobase regime. To confirm the validity of these simulations, when, after a few cycles, the wave activity becomes close to steady, the simulation results are compared to the oft-used linear fluid models for steady waves reviewed in the Appendix A. L20 also discussed the roles of the heavy and light species in a two-component atmosphere, and, based on MAVEN data, Williamson et al. [5] suggested plotting the vertical dependence in a multi-component atmosphere via the respective column densities. However, in order to clarify the effects in the exobase regime, here we simulate a very simple single-component 1D O atmosphere vs. altitude, with no horizontal flow, in order to examine the effect of using MK simulations and to readily compare the results to the analytic solutions. Of course, in a real atmosphere, wave activity is multi-component and multi-dimensional. In addition, the vertical behavior is roughly insensitive to the horizontal wavelength only at the Brunt–Väisälä (BV) frequency, the frequency of adiabatic oscillations. However, if the horizontal wavelength is very much larger than the vertical wavelength, 1D solutions can approximate aspects of the vertical behavior for a range of frequencies and altitudes. Although only acoustic and evanescent waves can be produced in 1D (Appendix A), the results described below are a crucial first step in simulating the transient and nonlinear effects of wave propagation into the exosphere.

2. Simulations

1D DSMC simulations of vertical acoustic (AW) and evanescent (EW) waves were carried out in a model single-species O atmosphere using Mars's gravity. For an atmosphere that is initially stationary (vertical flow speed $w = 0\ m/s$) and isothermal at temperature T_0, wave-like fluctuations were stimulated at the lower boundary of the simulation domain at a number of driving frequencies ω. Because the perturbed atmosphere exhibits variable vertical flow, the upper boundary of the simulation domain was treated as in L20. That is, in the more common DSMC simulations of static planetary atmospheres, molecules that move above the exobase with insufficient energy to escape are simply reflected at the upper boundary of the domain. In our simulations, such particles are returned and reenter the domain at the appropriate time. In this way, the effect of waves can be described at altitudes

in which collisions are rare. For simplicity, O + O collisions were implemented as in L20 with an average collisional cross-section of $\sigma = 4.5 \times 10^{-16}\ cm^2$ in the temperature range ($T_0 \sim 220 - 320\ K$) using the speed and angular dependence from [16]. The simulation domain was subdivided into either a 55- or 200-cell grid with variable grid size. At the domain's lower boundary (z_0 = 100 km), waves were initiated by creating an upward flux of new particles, with returning particles crossing the lower boundary removed. At the upper boundary (450 km), particles were returned at the appropriate time into the simulation domain as described above. For the L20 simulation, parameters with a 200-cell grid (marked * in Table 1), a comparison with the 55-cell grid, found results to be generally consistent above the lowest few cells. Therefore, 55 cells were used in all other cases presented here, with quantitative comparisons kept above 150 km to avoid any issues with the method implementing wave activity at the lower boundary.

The simulations were run for a time t_i sufficient to obtain a steady-state, isothermal O atmosphere (t_i~1000–2000 s). Waves were subsequently initiated by sinusoidally varying the upward flux Φ_+ of new particles across the lower boundary z_0 at constant temperature T_0 with an average number density $n_0 = \frac{\rho(z,t)}{m}$ at z_0, where $\rho(z,t)$ is the mass density and $m = 16$ u, the mass of atomic oxygen:

$$\Phi_+ = \frac{n_0 \langle v_0 \rangle}{4} \{1 + A_{0+} f(t) \sin[\omega(t - t_i)]\} \quad (1)$$

Here, $\langle v_0 \rangle$ is the mean thermal speed at T_0, and $\frac{n_0 \langle v_0 \rangle}{4}$ is the upward flux in the steady-state atmosphere. A_{0+} is the amplitude variation of the upward flux at the lower boundary, and $f(t)$ turns on the wave action at t_i and then off at t_f, which, in L20, had the form

$$f(t) = \begin{cases} 1, & | \quad t_i \le t \le t_f \\ 0, & | \text{ otherwise} \end{cases} \quad (2)$$

Beyond the time t_f, when the perturbation was terminated, the relaxation of the atmosphere was tracked as it slowly returned to the isothermal state. This was rapid near the lower boundary but required a number of periods at the background exobase and on into the corona. For comparison, the wave amplitude at the lower boundary was gradually—not abruptly—increased under conditions identical to Case (*) in Table 1 using a form assumed in [17]:

$$f(t) = \begin{cases} 1 - \exp\left[-\left(\frac{\omega}{2\pi}\right)(t - t_i)\right], & | \quad t_i \le t \le t_f \\ 0, & | \text{ otherwise} \end{cases} \quad (3)$$

Although the initial transients differed, the two simulations reached roughly the same steady behavior in about two cycles. Rather than arbitrarily choosing a form for the initial transient, wave activity for all cases discussed below was initiated using $f(t)$ in Equation (2), as in L20, in order to be consistent when describing the response.

To compare with the LAFM results, A_{0+} was chosen such that thermal escape was negligible. L20 showed that the vertical dependence scaled very roughly with the size of A_{0+} for $0.1 < A_{0+} < 0.25$ in Equation (1). Here, we give results for $A_{0+} = 0.25$, but, as in L20, we comment on simulations using $A_{0+} = 0.15$ in the discussion. Using $A_{0+} = 0.25$ in Equation (1) corresponds to a surface density amplitude of ~0.16 in the LAFM approximation, as discussed in the Appendix A. This is a reasonable density amplitude [2–4] which, of course, grows with altitude for an AW, consistent with density amplitudes seen in the exobase region of Mars [2], which can become up to ~50% of the background density [5].

Unless otherwise specified, the background simulation parameters used for the results in the figures below and in Table 1 are: ratio of specific heats $\gamma = \frac{5}{3}$; temperature $T_0 = 270\ K$; speed of sound $c_s = \left(\frac{\gamma k T_0}{m}\right)^{0.5} = 0.483\ km/s$; and nominal, steady-state exobase altitude $\Delta z_{ex} = z_{ex} - z_0 = H_0 \ln\left(2^{0.5} n_0 \sigma H_0\right) = 130\ km$ above the lower boundary. Similarly,

at the lower boundary ($z_0 = 100\ km$), the following values are used unless otherwise specified: number density $n_0 = 10^{16}\ O/m^3$; Mars gravity $g = 3.51\ m/s^2$; scale height $H_0 = \frac{kT_0}{mg} = 40\ km$; acoustic cutoff frequency $\omega_a = \left(\frac{\gamma}{2}\right)\left(\frac{g}{c_s}\right) = 6.05\ x\ 10^{-3}\ rad/s$; wave amplitude $A_{0+} = 0.25$; and wave action $f(t)$ per Equation (2) for five consecutive periods. For all results, minor smoothing to the data sets was applied as per the L20 technique. Table 1 gives key simulation results for steady wave activity using the above parameters. Changing the background temperature in our simulations from 270 K to 220 K and 320 K affected the details but not the nature of the results described below. Likewise, using twice the number density did not affect the qualitative behavior of the simulations and is not discussed further.

3. Results and Comparisons

The pressure, density, and temperature results are given as

$$\{\ p(z,t) = p_0(z) + p_1(z,t)\ ;\ \rho(z,t) = \rho_0(z) + \rho_1(z,t)\ ;\ T(z,t) = T_0(z) + T_1(z,t)\ \},$$

where $\{\ p_0(z)\ ;\rho_0(z)\ ;\ T_0(z)\ \}$ are the background values at altitude z and $\{\ p_1(z,t)\ ;\ \rho_1(z,t)\ ;\ T_1(z,t)\ \}$ are the perturbed time- and altitude-dependent contributions. The time-dependent ratios discussed below are $\left\{\ \frac{p_1(z,t)}{p_0(z)};\ \frac{\rho_1(z,t)}{\rho_0(z)}\left(=\frac{n_1(z,t)}{n_0(z)}\right);\ \frac{T_1(z,t)}{T_0(z)}\ \right\}$. Note that all calculations incorporating background values such as $p_0(z),\ n_0(z), \rho_0(z),\ T_0(z),\ w_0(z)$ use the actual simulated steady-state values at z prior to the onset of wave activity, which only differs from their theoretical counterparts, such as $n_0,\ T_0$, by less than 1%. The quantities $\left\{\ w, \frac{p_1}{p_0}, \frac{\rho_1}{\rho_0}, \frac{T_1}{T_0}\ \right\}$ for the LAFM are written as amplitudes and phases in the Appendix A. Those results for the oscillatory and vertical behavior of both 1D AW ($\omega > \omega_a$) and 1D EW ($\omega < \omega_a$) activity can be characterized by the quantity $\beta = 2H_0|k_z|$, with the magnitude of the vertical wavenumber $|k_z| = \frac{\left|\omega^2 - \omega_a^2\right|^{0.5}}{c_s}$. This corresponds to a wavelength $\lambda_z = \frac{2\pi}{k_z}$ for AWs, whereas EWs have an essentially infinite vertical wavelength. Since the simulations describe the transient as well as steady wave activity, the lower boundary conditions are discussed further in the Appendix A. Table 1, which is referred to extensively below, summarizes results of sample driving frequencies initiated under the background conditions given above.

Figure 1 gives DSMC results showing the variation in the atmosphere properties vs. time and altitude produced by an AW (Figure 1a,c) and an EW (Figure 1b,d), Cases (*) and (†) in Table 1, respectively. Figure 1a,b show that the vertical and transient behaviors for the two waves differ as expected. Whereas the density and temperature amplitudes of an AW grow significantly with altitude, as described quantitatively below, the EW amplitudes do not. The dashed horizontal lines mark the nominal exobase (230 km) for the initial background atmosphere. Figure 1c,d exhibit the variability at the nominal exobase in the density, temperature, and pressure amplitudes (left axis), and the vertical flow velocity $w(z,t)$ (right axis) due to the onset of wave activity. The difference in phases between the density and temperature for the AW was found to have a similar dependence on the background parameters in the collisional regime as in the LAFM. However, as shown in L20, the extraction of temperature using only the density data, as often carried out using spacecraft density data, is problematic. For instance, the temperature amplitude is seen to be always smaller than the density amplitude, unlike what is sometimes found using density data along a spacecraft's path. Results for simulations of other AWs with different background T_0 and surface densities showed that the resulting oscillatory behavior and phase differences under steady wave activity were moderately affected by collisions, changing very roughly according to the parameters in the LAFM. On termination of the driving frequency after five periods, wave activity near the exobase, unsurprisingly, persisted for a number of cycles (Figure 1c,d). Therefore, as is well understood, the typical interpretation of spacecraft density data can be problematic unless the activity is steady.

Table 1. Simulation results discussed for steady wave activity.

Wave Type	ω $[10^{-3} rad/s]$	β=2H_0 | k_z | $[rad]$	$c_{230/150}$	$(\frac{d\langle T_1\rangle}{dz})_{150-230}$ $[K/H_0]$
EW †	3.17 (=0.52 ω_a)	0.85	0.01	<0
EW ‡	5.92 (=0.98 ω_a)	0.20	0.70	4.9
AW *	9.50 (=1.57 ω_a)	1.21 (λ_z = 414 km)	0.90 (c_{ex}= 0.92)	9.4
AW	19.0 (=3.14 ω_a)	2.98 (λ_z = 169 km)	0.50 (c_{ex}= 0.74)	4.4

Case (†): EW case shown in Figure 1b,d and Figure 2b; as discussed below, it exhibits a small level of cooling in collisional regime but remains slightly warmer in the corona in Cycle 5 (i.e., near steady state). **Case (‡):** EW at lower boundary, becoming AW-like in exobase regime due to decreasing g and increasing average c_s; ω at the lower boundary is equivalent to the Brunt–Väisälä frequency (of interest only in 2D): $\omega_g = (\gamma-1)^{0.5}\left(\frac{g}{c_s}\right) = 0.980\,\omega_a$. **Case (*):** AW case shown in Figures 1a,c, 2a and 3, with parameters used in L20 for an O atmosphere (incorrectly referred to in L20 as the BV frequency). ω_a : acoustic cutoff frequency evaluated at the lower boundary. $c_{230/150}$**:** value of c in the expression $\exp\left[\frac{c(z-150\ km)}{2H_0}\right]$ for the growth of the density amplitude from 150 km up to the background exobase ~230 km; estimated from Figure 2 near steady wave activity. c_{ex}**:** theoretical estimate for an AW evaluated at the exobase using Equation (A7). $\left(\frac{d\langle T_1\rangle}{dz}\right)_{150-230}$**:** estimate of slope of the cycle averaged temperature amplitude from 150 to 230 km using Cycle 5 (i.e., near steady wave activity).

For steady wave activity in the LAFM approximation (Equations (A3)–(A5)), the temperature/density amplitude ratio is: $\frac{a_T}{a_\rho} = (\gamma-1)$ for an AW and $\frac{a_T}{a_\rho} = (\gamma-1)\frac{(1-\beta)}{(1+\beta)}$ for an EW, independent of altitude. For the cases in Figure 1, these are 0.67 and 0.054, respectively, exhibiting a similar trend to approximate steady values in the simulations at the nominal background exobase, ~0.4 and ~0.1, with the differences due to the molecular nature of the simulations. For the AW in Figure 1c, although the phases and the relative amplitudes differ from those in the LAFM, their variations with β are also similar. However, the temperature amplitude does not oscillate about zero at the nominal exobase. Rather, the cycle-averaged value is shifted upward, indicating, as expected, that net heating has occurred. Depending on the altitude, this added heat requires a number of cycles to dissipate after the wave activity ceases. Of course, heating does not occur in the LAFM, which is also the case for more elaborate linear models that include first-order viscosity and thermal conductivity terms (e.g., Equation (A5)). In those descriptions, heating is a second-order effect separately calculated using solutions to linear models, e.g., [18,19]. In MK simulations, however, it is a direct outcome as seen in Figure 1c.

Figure 1b,d give the results for a 1D EW, and similar behavior is seen when simulations are carried out at the other background temperatures. Because of the longer period, the pressure and density amplitudes are similar in size and nearly in phase. The small temperature amplitude seen in Figure 1d indicates that the gas is much closer to being equilibrated locally. Not only is the temperature amplitude a small fraction of the density amplitude, but the flow velocity and temperature are seen to be about $\frac{\pi}{2}$ and π out of phase with the density amplitude, consistent with the LAFM in Equation (A5).

Figure 2a,b show the transient growth vs. altitude of the peaks in the density amplitude from 150 km to 300 km for the AW and EW simulations in Figure 1. Each of the five density amplitude peaks across this altitude range is displayed as a ratio to the corresponding peak at ~150 km. As is well known, in the absence of viscosity and thermal conduction, the expected growth in the density amplitude of an AW is $\frac{\rho_1}{\rho_0} \sim \exp\left[\frac{(z-150km)}{2H_0}\right]$, as seen in the Appendix A. Therefore, dashed lines having the form $\exp\left[\frac{c(z-150\ km)}{2H_0}\right]$ are drawn to guide the eye. The coefficient c, indicating the growth with altitude, is seen to vary in time as steady state is approached. Near steady state (Peak 5), the difference from c = 1 for the activity driven by an AW is, of course, due to the inclusion of molecular

collisions accounting for the effect of viscosity and thermal conductivity. Therefore, the values of c for Peak 5 at the nominal exobase, written as $c_{230/150}$, are given in Table 1, above. Results for simulations at other background temperatures were roughly consistent with those displayed.

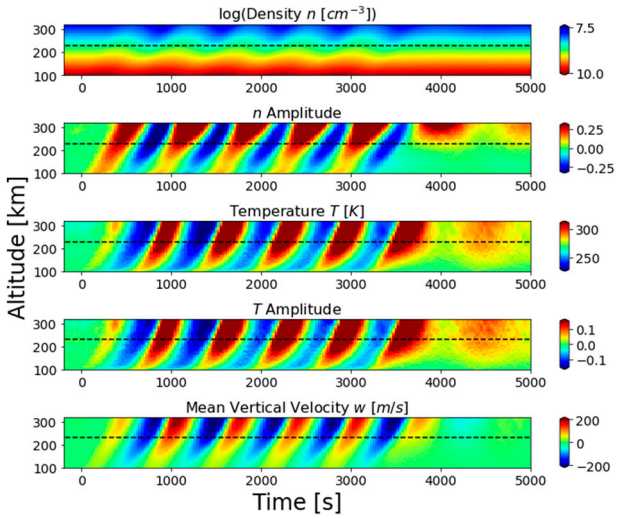

(**a**) AW* vertical and temporal evolution.

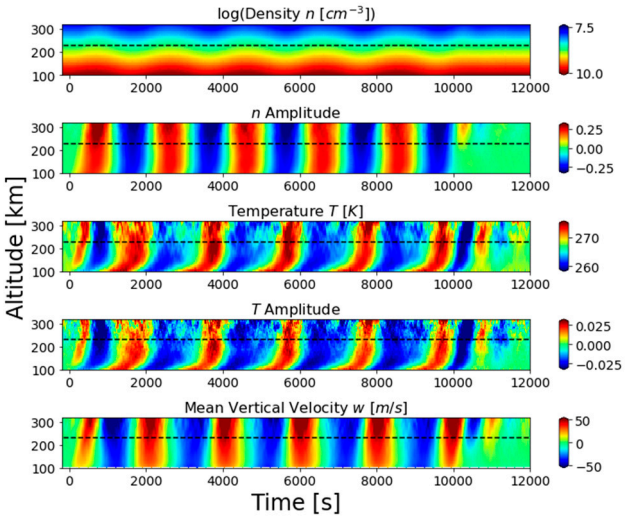

(**b**) EW† vertical and temporal evolution.

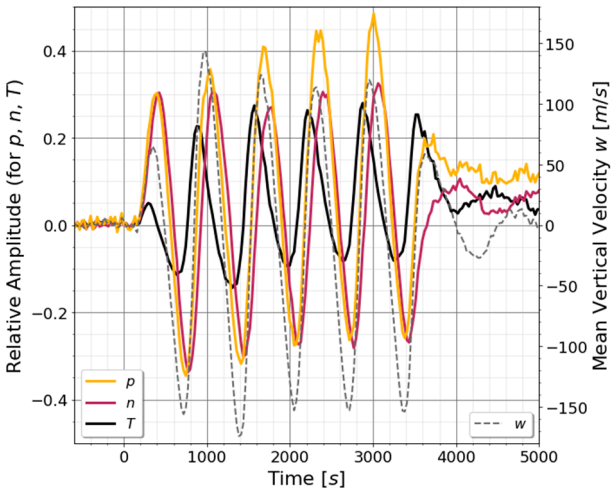

(**c**) AW* amplitudes at background exobase.

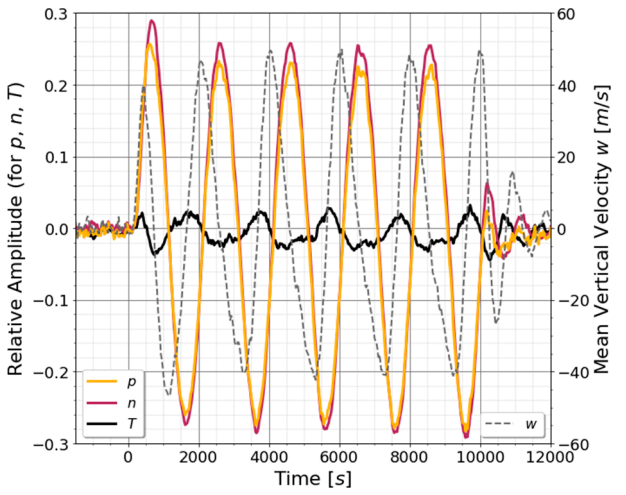

(**d**) EW† amplitudes at background exobase.

Figure 1. AW and EW activity driven at the lower boundary as in Equation (1), with $f(t)$ as in Equation (2) and $A_{0+} = 0.25$ for 5 periods after a steady-state isothermal atmosphere was achieved. Results: (**a**,**c**) Case (*) in Table 1 with 200 cells; (**b**,**d**) Case (†) in Table 1 with 55 cells. In (**a**,**b**): amplitudes (color scales) vs. altitude and time: dashed lines indicate nominal exobase for background atmosphere. In (**c**,**d**): amplitudes vs. time at nominal background exobase (230 km): solid curves left axis, dotted right axis. Note: for the AW in (**c**), net heating is indicated as the cycle-averaged temperature amplitude (red) is greater than zero; in (**d**), fluctuations in the small temperature amplitude indicate the size of uncertainties.

For an initial isothermal atmosphere with scale height H_0, the AW amplitude in the LAFM grows exponentially with a scale height $2H_0$ (i.e., $c = 1$) as discussed above, whereas the amplitude for an EW is predicted to grow more slowly (i.e., $c = 1 - \left[1 - \left(\frac{\omega}{\omega_a}\right)^2\right]^{0.5}$), as shown in the Appendix A. However, the simulation results in Figure 2 indicate that, following the onset of wave activity, the transient amplitudes (the amplitudes of the

sequential peaks), unsurprisingly, exhibit a very different behavior with altitude than the roughly steady wave values for both AW and EW. Therefore, in modeling wave activity, it is, again, clear that interpreting the density data vs. altitude along a spacecraft trajectory can be very problematic when the activity is variable.

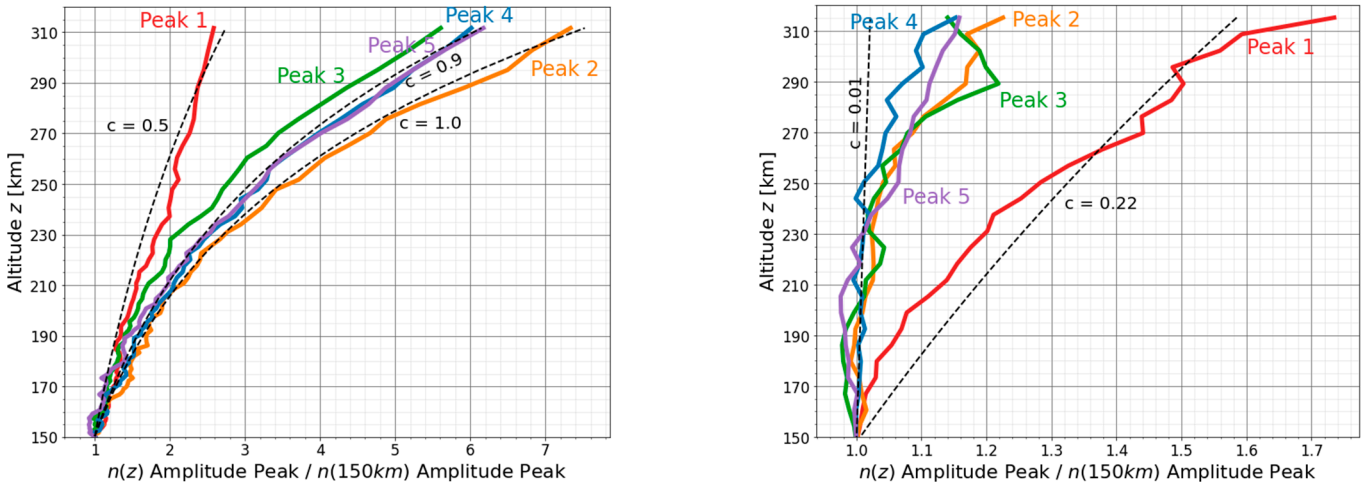

(**a**) AW * (**b**) EW †

Figure 2. Growth in density amplitude peaks vs. altitude (km) divided by the respective density amplitude peak at 150 km, i.e., $\frac{\rho_{1,\mathrm{peak}}(z)/\rho_0(z)}{\rho_{1,peak}(150\ km)/\rho_0(150\ km)}$. Dashed lines of the form $\exp\left[\frac{c(z-150\ km)}{2H_0}\right]$ are provided *as a guide*, with H_0 being the isothermal background scale height. (**a**) Case (*) in Table 1 ($c = 1$ in LAFM): 1st peak ($c \sim 0.5$), 5th peak ($c \sim 0.9$). (**b**) Case (†) in Table 1 ($c = 0.032$ in LAFM): 1st peak (c~0.2) with rapid decay in the growth in the collisional regime, but slow decay above the nominal background exobase (230 km). Fluctuations indicative of uncertainties in peak positions.

Following the onset of wave activity for the AW Case (*) in Table 1, above, the growth with altitude of the amplitude peaks in Figure 2a approaches a rough steady state very differently than for the EW in Figure 2b. Although the amplitude of the first pulse for an AW exhibits a growth with altitude much less than that predicted by the LAFM (c~0.5 vs. $c = 1$), c increases to ~0.9 by the fifth peak as steady activity is approached, indicating that the effect of viscosity and thermal conductivity is not large. However, when doubling that frequency, we found that c is about 0.2 for the initial peak, whereas the result given in Table 1 for the fifth peak is ~0.6. Therefore, the dissipative effect produced by simulating the molecular interactions is much larger at the higher frequency.

Following the onset for the EW case (†) in Table 1, the wave amplitude initially grows significantly with altitude. Although the initial growth with altitude is smaller, it is not unlike that of the initial AW peak. This is especially the case above the exobase, emphasizing the importance of understanding wave transients and variability. As the simulated EW approaches steady wave activity, the growth rapidly decays in the collisional regime, for which the LAFM predicts $c = 0.032$. However, the perturbation in the exosphere is seen to approach a steady state value very slowly.

When $\omega = 0.98\ \omega_a$ at the lower boundary (Case (‡) in Table 1, above), the scale factor c was again transient. It was ~0.4 at the first peak but in one period became ~0.7, very close to the $c_{230/150}$ value given in Table 1, above, but somewhat lower than the LAFM value c~0.8. Reducing A_{0+} to 0.15, changing the temperature, or increasing the density at the lower boundary changed the magnitude, but not the trends, in these results.

The c_{ex} values, also given in Table 1 above, are estimates of c at the exobase for AWs calculated using Equation (A7). The expression in Equation (7) was derived from the linear fluid model given in Equation (A5) in the Appendix A. This model includes, to first order, the viscosity and thermal conductivity, which are assumed to be small. It is seen that

these values, evaluated at the nominal background exobase, exhibit a trend similar to the near-steady-state simulation results ($c_{230/150}$) shown for the AWs in Table 1. This confirms that the collisional damping described in these simulations is consistent with fluid models and can affect the interpretation of observations of wave amplitude growth.

4. Heating

Since atmospheric temperatures are not directly measured by the Cassini or MAVEN spacecraft, the approximate temperature vs. altitude profiles on Titan and Mars are typically extracted from the 1D density data, e.g., [1,8]. The fact that the density and temperature peaks are out of phase, as seen in Figure 1, suggests that this procedure might be problematic, as mentioned above. Earlier, we used a 2D LAFM model to show that, in the presence of wave activity, this extraction procedure is useful only over a limited range of wave parameters [10]. L20 also used their 1D DSMC results to discuss this extraction method for atmospheres containing both one and two species. In the following, we discuss the heating seen in these simulations.

Consistent with the observation of reduced exponential growth of the density amplitude (i.e., Figure 2 and $c_{230/150}$ in Table 1 above), the implementation of molecular collisions also affects the temperature vs. altitude for an AW. Unlike in linear fluid models that include viscosity and thermal conduction, e.g., [18], the effect on the temperature vs. altitude is a direct outcome of MK simulations, as also seen in Figures 1c and 3a, and as mentioned earlier. That is, as an atmosphere is perturbed by the initiation of an acoustic wave, $\frac{T_1}{T_0}$ gradually deviates from an oscillation about zero to an oscillation about a value that increases with time and with altitude, indicative of heating. For the case shown in Figure 3a, the cycle-averaged shift in temperature, $\langle T_1 \rangle$, grows over the indicated altitude range from ~6 K to ~40 K. For those AWs simulated, we also found that the size of $\langle T_1 \rangle$ increases nearly linearly with altitude in this region of the atmosphere. Column 5 in Table 1 above gives an estimate of the near steady state, simulated, cycle-averaged change in temperature $\langle T_1 \rangle$ over the background scale height in the exobase region. These values were estimated using the fifth perturbation cycle. While the AW cases exhibit significant heating, as expected, the EW for Case (†) exhibits very slight cooling. It is interesting, however, that when $\omega = 0.98\ \omega_a$ at the lower boundary for Case (‡) in Table 1, above, ω begins to exceed the acoustic cutoff frequency as the altitude increases. Therefore, in the exobase regime, the cycle-averaged temperature $\langle T_1 \rangle$ is seen to have increased significantly, similar to the AWs that have much higher frequencies at the lower boundary. The observed growth in the cycle-averaged temperature for thid case was also found to increase nearly linearly with altitude.

For the amplitudes used here, such increases in $\langle T_1 \rangle$ do not cause significant Jeans escape of O but can affect the escape of the often concomitant, lighter species H_2, as well as affect the local atmospheric chemistry. However, Figure 3b shows that the increase in T with altitude can significantly affect the density amplitude above the nominal background exobase, a process suggested by MAVEN data [2,5]. Below the nominal background exobase in these simulations (~230 km), the density amplitudes are close to LAFM predictions, as in Figure 1c. However, above the exobase, the cycle-averaged heating has a significant effect on not only the density amplitude but also the cycle-averaged density (~20%) as steady activity is approached. Such an increase can affect the interaction of the molecules driven into the corona by wave activity with the ambient space plasma. These interactions are a principal driver of escape on Mars and Titan, e.g., [1,20]. This increase is often suppressed in fluid models by the assumed upper boundary conditions, but is a natural outcome of the MK simulations. Of course, in 2D, the variable and enhanced perturbations above the nominal exobase can eventually be dispersed by ballistic transport and wave saturation, e.g., [5]. However, our simulations also show how the perturbations propagating into the coronal region dissipate only slowly after the wave activity at the lower boundary ceases. This can significantly alter the interpretation of spacecraft data when fluid models for steady wave activity are used to fit the data, which is often the case.

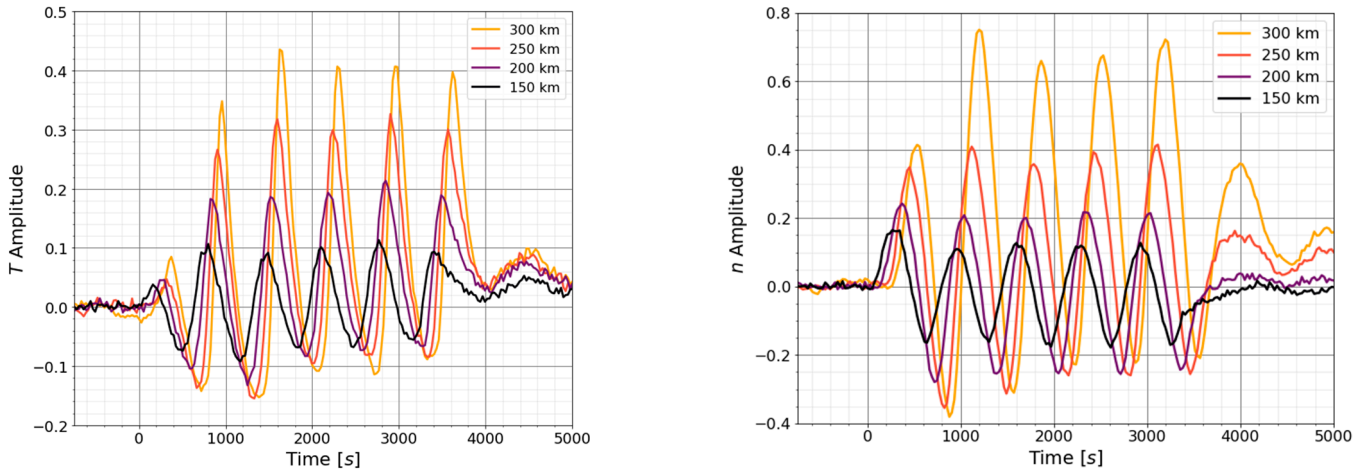

(**a**) AW * temperature amplitude.

(**b**) AW * density amplitude.

Figure 3. For AW Case (*) in Table 1, temperature and density amplitudes vs. time (as in Figure 1c) at a number of altitudes: (**a**) $\frac{T_1}{T_0}$, and (**b**) $\frac{n_1}{n_0}$. The cycle-averaged density above the nominal background exobase is seen to increase significantly.

The temperature increases in Table 1 for AWs, as well as those calculated for $A_{0+} = 0.15$ and other background temperatures and densities at the lower boundary, were found to roughly scale with amplitude squared and with ω^{-1} when $\left(\frac{\omega}{\omega_a}\right)^2 \gg 1$. In these simulations, heating is primarily due to the forcing of the gas in a gravitational field, and the net cooling during steady activity is primarily due to the downward flow across the lower boundary. Whereas low-frequency waves can approach nearly adiabatic transport, the much more rapid forcing by the AWs causes compression and mixing of gas with different temperatures and densities vs. altitude. In fluid models, those heating effects are described by a number of second-order terms in the heat equation, with the dominant contribution for the parameters here being the divergence of the sensible heat flux [19].

5. Summary

We expanded here on the results presented in Leclercq et al. [13] in order to demonstrate the usefulness of molecular kinetic (MK) simulations for describing the effect of wave activity in the rarefied region of a planetary atmosphere. Such simulations are essentially equivalent to solving the Boltzmann equation [15,21]. The significant and variable wave activity observed in the exobase regions of Titan and Mars, which is of considerable interest, e.g., [2,7], does not appear to significantly affect the thermal escape of the dominant constituents, e.g., [7,8]. However, we show that such activity does affect the population and extent of the atmospheric corona, which in turn determines its interaction with the space environment.

Below the exobase and near steady activity, the resulting density amplitudes are shown to be roughly consistent with those predicted by 1D steady wave activity models in the Appendix A. Allowing for conditions that are typically applied at the lower boundary, any differences in the phases and amplitudes are, of course, due to the direct inclusion of molecular collisions. However, in the region from which escape can occur, these simulations exhibit significant differences from fluid models. In addition, as discussed above, the temperature profiles are a direct outcome of the simulations, which were seen to increase nearly linearly with altitude for AWs propagating to the exobase. These 1D results, therefore, indicate that molecular simulations are needed to improve our understanding of the effect of gravity waves driven from below on the exobase region and on the content of the extended corona of a planet's atmosphere. These are regions of the atmospheres on

planetary bodies often studied by spacecraft in situ, or by remote sensing of auroral activity, but often not accurately modeled using fluid dynamics.

The results presented also show the importance of understanding the transient behavior in a highly variable atmosphere by simulating the onset and decay of wave activity in a thin atmosphere driven from below. Such variability can also be introduced by a transient heat pulse in the thermosphere driven externally by solar activity or by the ambient plasma, as considered in L20. Although we examined a range of amplitudes at the lower boundary, as suggested by observations in the upper atmosphere of Mars, e.g., [2,5,22], for emphasis, we primarily presented results for a flux amplitude at the lower boundary of 0.25, our largest value for which escape is still negligible. As described, this corresponds to a significant but realistic density amplitude at the lower boundary of ~0.16 [2,3]. Figures 1 and 3 show that the transient wave activity persists in the extended corona for a number of cycles beyond the termination of wave activity at depth. When using only density observations of waves vs. altitude, this can affect the interpretation of wave type and, therefore, the estimates of the net heating. Figure 2 also shows that, near the onset of wave activity, it can also be difficult to separate an EW disturbance from an AW disturbance without additional information on the horizontal structure or frequency of the perturbation. Such data is often not available from in situ spacecraft measurements. Finally, MK simulations are useful as they also directly determine the nonlinear effects on the amplitudes and phases in the rarefied region, as well as on the heating vs. altitude, a principal goal of the considerable literature on wave activity, e.g., [8].

Although it is unlikely that highly perturbed upper atmospheres can be described as having an isothermal background, or that the activity can be approximated using steady-state models in a highly variable atmosphere such as that on Mars, such assumptions are often made. However, it is clear that transients and atmospheric variability can be readily incorporated into MK simulations when describing the propagation of wave energy into the region of a planetary atmosphere that transitions from collision-dominated to a nearly collisionless corona.

Of course, when wave activity occurs over many scale heights, an MK model would need to be coupled to a fluid model from below for computational efficiency [23]. Although the background gravity, temperature, and density used are Mars-like, consistent with L20, the vertical wavelengths initiated are relatively long in our simple O upper atmosphere. Therefore, this work is intended to show the effects revealed by using a molecular model to describe the propagation of wave energy into the exobase regime. Of course, wave activity in a real atmosphere requires multi-dimensional, multi-component MK simulations, which are now underway.

Author Contributions: Conceptualization, R.E.J.; methodology & software, L.T., O.J.T. and A.K.W.; validation, L.T., O.J.T. and H.N.W.; formal analysis and investigation, R.E.J. and H.N.W.; data curation, L.T.; writing—original draft preparation, R.E.J.; writing—review and editing, L.T., O.J.T., H.N.W. and S.R.C.M.; visualization, L.T. All authors have read and agreed to the published version of the manuscript.

Funding: This research received no external funding.

Conflicts of Interest: The authors declare no conflict of interest.

Appendix A

Appendix A.1. 1D Linear Analytic Fluid Model (LAFM) for Steadily Driven Waves

The continuity, momentum, and energy propagation equations from Hines [24], which ignore viscosity and thermal conductivity, are reduced to 1D:

$$\begin{gathered} \frac{\partial \rho_1}{\partial t} - w\frac{\rho_0}{H_0} + \rho_0 \frac{\partial w}{\partial z} = 0 \\ \rho_0 \frac{\partial w}{\partial t} = -\frac{\partial p_1}{\partial z} - \rho_1 g \\ \frac{\partial p_1}{\partial t} - w\frac{p_0}{H_0} = c_s^2\left(\frac{\partial \rho_1}{\partial t} - \rho_0 \frac{w}{H_0}\right) \end{gathered} \tag{A1}$$

In the above equations, $\{p_0(z), \rho_0(z), T_0\}$ and $\{p_1(z), \rho_1(z), T_1\}$ are the background and perturbed pressures, mass densities, and temperatures, respectively; w is the vertical flow speed; and z is the altitude above the lower boundary z_0 (assumed here to be $z_0 = 0$ for simplicity). Assuming the unperturbed, 1D, single-species atmosphere with initial flow $w = 0$ is isothermal at temperature T_0, we write $\frac{\rho_0(z)}{\rho_0(0)} = \frac{p_0(z)}{p_0(0)} = \exp\left(-\frac{z}{H_0}\right)$, where $H_0 = \frac{kT_0}{mg}$ is the scale height and m is the molecular mass. With the ratio of specific heats γ and speed of sound $c_s = \left(\frac{\gamma k T_0}{m}\right)^{0.5}$, the acoustic cutoff frequency is $\omega_a = \left(\frac{\gamma}{2}\right)\left(\frac{g}{c_s}\right) = \left(\frac{\gamma g}{4H_0}\right)^{0.5}$. Such a 1D atmosphere steadily driven at a frequency ω can produce waves representative of acoustic and evanescent waves but not internal gravity waves. Solutions to Equation (A1) for steady wave activity driven from below are presented for both AW and EW behavior. Substituting $F(z,t) = A(\omega)\exp(i\omega t - iK_z z)$ where $A(\omega)$ is a dimensionless amplitude at the lower boundary and K_z is a vertical wavenumber, the solutions in Hines (1960) can be written in the form of amplitudes a_i and phases ϕ_i relative to that for w:

$$\frac{p_1}{p_0} = a_p \exp(i\phi_p) F(z,t) \quad ; \quad \frac{\rho_1}{\rho_0} = a_\rho \exp(i\phi_\rho) F(z,t) \quad ; \quad w = (2H_0\omega) F(z,t) \tag{A2}$$

with $\frac{T_1}{T_0} \sim \frac{p_1}{p_0} - \frac{\rho_1}{\rho_0} = a_T \exp(i\phi_T) F(z,t)$. Substituting Equation (A2) into Equation (A1), the amplitudes and phases are given below.

AW ($\omega > \omega_a$):

For $k_z = \frac{\left[\left(\frac{\omega}{\omega_a}\right)^2 - 1\right]^{0.5}}{2H_0}$, $K_z = \frac{i}{2H_0} \pm k_z$, $\beta = 2H_0|k_z|$, and $F_\pm(z,t) = A_\pm \exp\left[\frac{z}{2H_0}(1 \pm i\beta)\right]$ $\exp[i\omega t]$, one obtains:

$$\begin{array}{c} a_p = \left[(\gamma\beta)^2 + (2-\gamma)^2\right]^{0.5} \quad ; \quad \phi_p = -\tan^{-1}\left(\frac{2-\gamma}{\beta\gamma}\right) \\ a_\rho = \left(\beta^2 + 1\right)^{0.5} \quad ; \quad \phi_\rho = -\tan^{-1}\left(\beta^{-1}\right) \\ a_T = (\gamma - 1) a_\rho \quad ; \quad \phi_T = \tan^{-1}\left(\beta^{-1}\right) \end{array} \tag{A3}$$

In this way, the density amplitude for an AW is predicted to grow as $\frac{\rho_1}{\rho_0} \sim \exp\left[\frac{c(z-z_0)}{2H_0}\right]$ with $c = 1$.

EW ($\omega < \omega_a$):

For $K_z = i\left[\frac{1}{2H_0} \pm |k_z|\right]$ and $|k_z| = \frac{\left[1 - (\omega/\omega_a)^2\right]^{0.5}}{2H_0}$, so that with $\beta \leq 1$ the bound-damped solution has the form $F_\pm(z,t) = A_\pm \exp\left(\frac{cz}{2H_0}\right)\exp(i\omega t)$, $c = (1-\beta)$ gives:

$$\begin{array}{c} a_p = [(2-\gamma) + \gamma\beta] \quad ; \quad \phi_p = -\frac{\pi}{2} \\ a_\rho = 1 + \beta \quad ; \quad \phi_\rho = -\frac{\pi}{2} \\ a_T = (\gamma - 1)(1 - \beta) \quad ; \quad \phi_T = \frac{\pi}{2} \end{array} \tag{A4}$$

Therefore, the density amplitude for an EW is predicted to grow as $\frac{\rho_1}{\rho_0} \sim \exp\left[\frac{c(z-z_0)}{2H_0}\right]$, with $c = 1 - \left[1 - \left(\frac{\omega}{\omega_a}\right)^2\right]^{0.5}$.

For both waveforms above, the temperature amplitude is proportional to the density amplitude, and $\beta \to 0$ as $\omega \to \omega_a$ so that the solutions merge. Although the EW frequencies simulated here in 1D are instructive, they only crudely represent low-frequency wave activity below the Brunt–Väisälä frequency $\omega_g = (\gamma - 1)^{0.5}\left(\frac{g}{c_s}\right)$.

The linear approximation can be expanded upon to include the molecular viscosity μ and thermal conductivity K, assuming to first-order that they depend primarily on the background temperature T_0. Using equations reduced from [19] and ignoring eddy effects:

$$\begin{gathered} \frac{\partial\left(\frac{\rho_1}{\rho_0}\right)}{\partial t} + \frac{\partial w}{\partial z} - \frac{w}{H_0} = 0 \\ \rho_0 \frac{\partial w}{\partial t} + p_0 \frac{\partial\left(\frac{p_1}{p_0}\right)}{\partial z} - g\rho_0 \frac{T_1}{T_0} - \frac{4}{3}\mu \frac{\partial^2 w}{\partial z^2} = 0 \\ c_v \rho_0 \frac{\partial T_1}{\partial t} + p_0 \frac{\partial w}{\partial z} - \frac{\partial\left(K \frac{\partial T_1}{\partial z}\right)}{\partial z} = 0 \end{gathered} \tag{A5}$$

Dividing the momentum and energy equations in Equation (A5) by the background density and comparing to Equation (A1), the viscous and conduction terms affect the z-dependence. Therefore, rewriting $K_z z$ in Equation (A2) as $\int_0^z K_z dz\prime$, substituting those forms into Equation (A5), and keeping only linear terms, we obtain first-order solutions. Since the analytic analysis is tedious, we only give the AW result for K_z:

$$-i2H_0 \int_0^z K_z\prime dz \sim \left[z - \frac{x^3}{\beta}\int_0^z \alpha\left(z'\right)dz'\right] \pm (-i)\beta\left[1 + 2x\int_0^z \alpha\left(z'\right)dz'\right] \tag{A6}$$

with $x = \frac{\omega}{\omega_a}$; $\alpha(z) = \frac{1}{2}\left(\frac{\eta(z)}{2H_0 c_s}\right)\left[\frac{(\gamma-1)}{Pr} + \frac{4}{3}\right] = C\left(\frac{\eta(z)}{4H_0 c_s}\right)$; using $\eta(z) = \frac{\mu}{\rho_0(z)}$ and the Prandtl number Pr, the ratio of the momentum and thermal diffusivities. The diffusive effects are seen to lead to a change in the amplitude vs. altitude (imaginary term) and affect the phase shifts. Using the first term, we write the amplitude growth of $\frac{\rho_1}{\rho_0}$ as a function of altitude as in the main text in form $\exp\left(c\frac{z}{2H_0}\right)$. Based on Equation (A6), c becomes

$$c \sim [1 - \epsilon(z)], \text{ with } \epsilon(z) = \frac{x^3}{\beta}\int_0^z \alpha\left(z'\right)dz' \text{ when } \epsilon \ll 1 \tag{A7}$$

Based on values from [25] for atomic O, $\eta(z_{ex}) = 1.73 \times 10^6\ m^2/s$ and Pr $\sim \frac{2}{3}$ were used to estimate the AW c at the exobase via Equation (A7)–given in Table 1 as c_{ex}. These values are close to those estimated using our O + O collision cross-section.

Appendix A.2. Boundary Conditions for Simulations and LAFM

In our simulations, the upward flux is varied sinusoidally at the lower boundary with T_0 and n_0 fixed as in Equation (1), implying that $w(0,t) = \frac{n_0 v_0}{4} A_{0+} \sin[\omega(t - t_i)]$. A roughly steadily-driven wave with fixed amplitude at the lower boundary produces nearly steady wave activity in about an acoustic cutoff period, after which the amplitude is seen to increase with altitude above the lower boundary. In the LAFM solutions above, the phases are measured relative to w. To compare our near-steady-activity results, the amplitudes $\left\{\frac{\rho_1}{\rho_0}, \frac{p_1}{p_0}, \frac{T_1}{T_0}\right\}$ in Equation (A3) at the lower boundary must be scaled by $\frac{\langle v_0\rangle}{4}\frac{1}{2H_0\omega}$. Therefore, the LAFM temperature amplitude for an AW becomes:

$$\left|\frac{T_1}{T_0}\right| \sim \frac{\langle v_0\rangle}{4}\frac{1}{2H_0\omega}(\gamma - 1)\left(\beta^2 + 1\right)^{0.5} A_{0+} \exp\left[\frac{c(z - z_0)}{2H_0}\right] \tag{A8}$$

where $c = 1$ in the absence of viscosity and thermal conductivity.

References

1. Snowden, D.; Yelle, R.V.; Cui, J.; Wahlund, J.-E.; Edberg NJ, T.; Ågren, K. The thermal structure of Titan's upper atmosphere, I: Temperature profiles from Cassini INMS observations. *Icarus* **2013**, *226*, 552–582. [CrossRef]
2. Yiğit, E.; England, S.L.; Liu, G.; Medvedev, A.S.; Mahaffy, P.R.; Kuroda, T.; Jakosky, B.M. High-altitude gravity waves in the Martian thermosphere observed by MAVEN/NGIMS and modeled by a gravity wave scheme. *Geophys. Res. Lett.* **2015**, *42*, 8993–9000. [CrossRef]

3. England, S.L.; Liu, G.; Yiğit, E.; Mahaffy, P.R.; Elrod, M.; Benna, M.; Nakagawa, H.; Terada, N.; Jakosky, B. Maven NGIMS observations of atmospheric gravity waves in the Martian thermosphere: Gravity wave observations at Mars. *J. Geophys. Res. Space Phys.* **2017**, *122*, 2310–2335. [CrossRef]
4. Terada, N.; Leblanc, F.; Nakagawa, H.; Medvedev, A.S.; Yiğit, E.; Kuroda, T.; Hara, T.; England, S.L.; Fujiwara, H.; Terada, K.; et al. Global distribution and parameter dependences of gravity wave activity in the Martian upper thermosphere derived from MAVEN/ NGIMS observations. *JGR Space Phys.* **2017**, *122*, 2374–2397. [CrossRef]
5. Williamson, H.N.; Johnson, R.E.; Leclercq, L.; Elrod, M.K. Large amplitude perturbations in the Martian exosphere seen in MAVEN NGIMS data. *Icarus* **2019**, *331*, 110–115. [CrossRef]
6. Wang, X.; Lian, Y.; Cui, J.; Richardson, M.; Wu, Z.; Li, J. Temperature variability in Titan's upper atmosphere: The role of wave dissipation. *JGR Planets* **2020**, *125*, e2019JE006163. [CrossRef]
7. Yiğit, E. Martian water escape and internal waves. *Science* **2021**, *374*, 1323–1324. [CrossRef]
8. Walterscheid, R.L.; Hickey, M.P.; Schubert, G. Wave heating and Jeans escape in the Martian upper atmosphere. *JGR Planets* **2013**, *118*, 2413–2422. [CrossRef]
9. Siddle, A.G.; Mueller-Wodarg IC, F.; Stone, S.W.; Yelle, R.V. Global characteristics of gravity waves in the upper atmosphere of Mars as measured by MAVEN/NGIMS. *Icarus* **2019**, *333*, 12–21. [CrossRef]
10. Johnson, R.E.; Woodson, A.K.; Tian, L.; Tucker, O.J.; Williamson, H.N. Temperature extraction from spacecraft density profiles in the presence of wave activity. *Icarus* **2021**, *357*, 114257. [CrossRef]
11. Volkov, A.N.; Johnson, R.E.; Tucker, O.J.; Erwin, J.T. Thermally driven atmospheric escape: Transition from hydrodynamic to Jeans escape. *ApJL* **2011**, *729*, L24. [CrossRef]
12. Tucker, O.J.; Waalkes, W.; Tenishev, V.M.; Johnson, R.E.; Bieler, A.; Combi, M.R.; Nagy, A.F. Examining the exobase approximation: DSMC models of Titan's upper atmosphere. *Icarus* **2016**, *272*, 290–300. [CrossRef]
13. Leclercq, L.; Williamson, H.N.; Johnson, R.E.; Tucker, O.J.; Tian, L.; Snowden, D. Molecular kinetic simulations of transient perturbations in a planet's upper atmosphere. *Icarus* **2020**, *335*, 113394. [CrossRef]
14. Tucker, O.J.; Johnson, R.E.; Deighan, J.I.; Volkov, A.N. Diffusion and thermal escape of H_2 from Titan's atmosphere: Monte Carlo simulations. *Icarus* **2013**, *222*, 149–158. [CrossRef]
15. Bird, G.A. *The DSMC Method, Version 1.2*; CreateSpace Independent Publishing Platform Erscheinungsort nicht ermittelbar: Exeter, UK, 2013; ISBN1 1492112909. ISBN2 9781492112907.
16. Lewkow, N.R.; Kharchenko, V. Precipitation of energetic neutral atoms and induced non-thermal escape fluxes from the Martian atmosphere. *APJ* **2014**, *790*, 98–112. [CrossRef]
17. Kurdyaeva, Y.A.; Kshevetshii, S.P.; Gavrilov, N.M.; Kulichkov, S.N. Correct boundary conditions for the high-resolution model of nonlinear acoustic-gravity waves forced by atmospheric pressure variations. *Pure Appl. Geophys.* **2018**, *175*, 3639–3652, Springer International Publishing AG, part of Springer Nature. [CrossRef]
18. Schubert, G.; Hickey, M.P.; Walterscheid, R.L. Heating of Jupiter's thermosphere by the dissipation of upward propagating acoustic waves. *Icarus* **2003**, *163*, 398–413. [CrossRef]
19. Schubert, G.; Hickey, M.P.; Walterscheid, R.L. Physical processes in acoustic wave heating of the thermosphere. *J. Geophys. Res.* **2005**, *110*, D07106. [CrossRef]
20. Lichtenegger HI, M.; Dyadechkin, S.; Scherf, M.; Lammer, H.; Adam, R.; Kallio, E.; Amerstorfer, U.V.; Jarvinen, R. Non-thermal escape of the Martian CO_2 atmosphere over time: Constrained by Ar isotopes. *Icarus* **2022**, *382*, 115009. [CrossRef]
21. Solovchuk, M.A.; Leble, S.B. One-dimensional ultrasound propagation at stratified gas: Gross-Jackson model. *Eprint Arxiv Phys.* **2006**. [CrossRef]
22. Medvedev, A.S.; Yiğit, E. Gravity waves in planetary atmospheres: Their effects and parameterization in global circulation models. *Atmosphere* **2019**, *10*, 531. [CrossRef]
23. Erwin, J.T.; Tucker, O.J.; Johnson, R.E. Hybrid fluid/kinetic modeling of Pluto's escaping atmosphere. *Icarus* **2013**, *226*, 375–384. [CrossRef]
24. Hines, C.O. Internal atmospheric gravity waves at ionospheric heights. *Can. J. Phys.* **1960**, *38*, 1441–1481. [CrossRef]
25. Dalgarno, A.; Smith, F.J. The thermal conductivity and viscosity of atomic oxygen. *Planet. Space Sci.* **1962**, *9*, 1–2. [CrossRef]